AIAA JOURNAL
Vol. 33, No. 11, November 1995

Hartmann Wave Front Sensor Studies of Dynamic Organized Structure in Flowfields

L. McMackin,* B. Masson,† and N. Clark‡
Phillips Laboratory, Kirtland Air Force Base, New Mexico 87117
and
K. Bishop,§ R. Pierson,¶ and E. Chen§
Applied Technology Associates, Inc., Albuquerque, New Mexico 87117

In this paper, the results of an investigation of a one-dimensional Shack–Hartmann wave front sensor are presented for measurement of an optical wave front after passage through a round low-speed jet. The sensor has a linescan rate of 2.2 kHz that resolves the passing vortical features of the developing jet flow. After a brief summary of the principles of Hartmann sensing, results of an experimental determination of the sensitivity limits of our particular wave front sensor are presented. Noise sources in Hartmann sensing are then reviewed, and results of a simulation are presented to show the influence of noise on the resolution limits of the Hartmann sensor. The relevance of the simulation results to the design of a 2.2-kHz, multiview, tomographic system based on Hartmann sensing is also discussed.

Nomenclature

f_L = focal length of lenslets
R_{max} = radius of curvature of flattest spherical wave that can be accurately measured by the detector
$\Delta\xi$ = lenslet spacing
ξ_i = location of center of lenslet i
σ_θ = rms noise tilt per lenslet

I. Introduction

THIS paper presents the results of an investigation into the optical performance characteristics of one-dimensional Shack–Hartmann wave front sensors[1,2] in the context of the study and control of the optical properties of unsteady fluid flows and turbulence. The flowfield under study is the initial region of a round, low-speed jet, certainly one of the canonical flows in fluid mechanics. Whereas knowledge of this flowfield is already comprehensive,[3] an investigation using a Shack–Hartmann sensor, which will be referred to simply as a Hartmann sensor, is still of interest for several reasons. One practical reason lies in the simplicity and economy of the wave front sensor itself, which consists of a commercially available lenslet array and a charged-coupled device (CCD) camera to track the focal spots of the lenslets and, in laboratory applications, a small semiconductor laser diode serving as the wave front source. Because of the pixelation of the CCD array in the camera, the output of the sensor is naturally digitized and easily stored for rapid access, processing, and distribution (our sensor data are available over the Internet to those who are interested). Perhaps the most compelling reason for interest in the wave front sensor is that these devices already play a pivotal role in the development of compensation systems for atmospheric turbulence in the new generation of ground-based telescopes.[4,5] In the atmospheric compensation application, the wave front sensor provides input to the deformable-mirror adaptive optics feedback loop achieving overall correction rates of several hundred hertz. This capability illustrates the natural compatibility between the digital output of the sensor and the on-line digital processors forming the optical control system.

Of particular interest to the authors is the potential for the development of multiple-view, high-speed optical tomography based on the Hartmann technique.[6] Such a system removes the line-of-sight integration drawback inherent in any single-view optical measurement. Our multiview results are only preliminary at this time and are not presented here. Because of the importance of tomography, however, selected results from our design studies of a fast, Hartmann-based tomographic system are presented in a brief section of this paper. Whereas optical tomography has been used previously to create three-dimensional flowfield visualizations, the necessary data to generate the tomographic reconstructions are often collected over a period of time that is long with respect to the convective time scale of flow structures. This results in a time-averaged reconstruction[7–10] of the flow where images of the instantaneous structures have been smeared out. Temporally resolved tomographic systems[11,12] have proven to be more complex. With Hartmann sensors, a two-dimensional optical tomographic system will operate at the CCD camera linescan rate of several kilohertz. High-spatial resolution is achieved by minimizing the lenslet size subject to the conditions of maintaining a low-noise and low-crosstalk environment. High-temporal resolution is obtained by limiting the data acquisition to linear measurements in a single plane.

As an optical flowfield investigation tool, Hartmann sensing is a variant of the thin-beam deflection technique.[13–16] Unlike thin-beam deflection, however, the sensitivity of the Hartmann measurement can be controlled. Because the magnitude of the deflection of the focal spots is proportional to the focal length of the lenslets [see Eq. (1)], an appropriate choice of the focal length can provide the necessary sensitivity. Another advantage of the Hartmann sensor is the ability to make a large number of separate jitter measurements from a single expanded optical beam as a result of the small size and closely packed arrangement of the lenslets in a one- or two-dimensional array.[17,18]

This paper begins with a brief introduction to Hartmann sensors in Sec. II. Section III describes test results for the sensitivity limits of the Hartmann sensor, and Sec. IV describes the sensor's noise characteristics. In Sec. V, the impact of sensor noise on a tomographic system is described. Section VI presents a comparison of flowfield measurements using the Hartmann sensor and anemometry.

Presented as Paper 94-2548 at the AIAA 18th Ground Test Conference, Colorado Springs, CO, June 20–23, 1994; received June 30, 1994; revision received April 10, 1995; accepted for publication May 17, 1995.

*Research Physicist, Imaging Technology Branch, Advanced Imaging Division. Member AIAA.
†Research Physicist, Flight Test Branch, Airborne Laser Technology Division. Senior Member AIAA.
‡Electronics Engineer, Imaging Technology Branch, Advanced Imaging Division.
§Optical Engineer.
¶Program Manager.

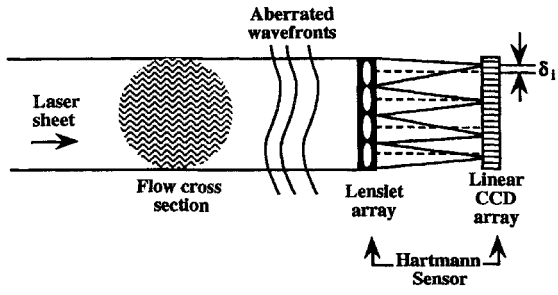

Fig. 1a Linear Hartmann sensor schematic; dashed lines indicate on-axis focal spot positions; flow induced phase disturbances produce focal spot deflections δ_i.

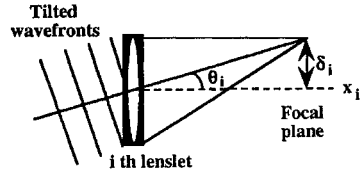

Fig. 1b Closeup of a single lenslet and a tilted wave-front shows the relation between θ_i and δ_i.

II. Hartmann Sensing

Hartmann sensing[19] offers a simple method of measuring the optical phase of laser light that has been transmitted though an aberrating medium. In general, a Hartmann sensor consists of an array of small lenses, called lenslets, a pixelated camera, and an algorithm that can locate the positions of the focal spot intensity patterns recorded by the camera. The lenslet array serves to separate a single laser sheet into a number of subapertures. The lenslets focus the light within each subaperture onto the camera, as shown in Fig. 1a. The sensor works on the principle that the focused spots in the focal plane of the lenslet array will be deflected away from their optical axes due to aberrations in the optical beam. The deflection distance δ_i is proportional to the local derivative of the optical wave front impinging on the lenslet array. Because light propagates in the direction normal to the wave front, the local derivative (or slope) of the wave front incident on a lenslet, given by angle θ_i, determines the local direction of propagation of the light to the focal plane (see Fig. 1b). In this way δ_i is related to θ_i by

$$\tan\theta_i \approx \theta_i = \delta_i / f_L \tag{1}$$

Thus, detecting the centroid position of the spot from each lenslet measures the gradient of the optical phase along the detector axis. Integration of this measurement along the detector axis direction yields the optical path differences (OPDs) experienced by the optical beam. For the general problem of wave front reconstruction see Ref. 19.

The one-dimensional Hartmann sensor used in our experiments is a two-component system consisting of a linear array of tiny cylindrical lenslets and a one-dimensional CCD array that is located at the back focal plane of the lenslets. The 2.5-cm-long lenslet array used in our experiments was designed and supplied to us with camera and software by Neal[18] of Sandia National Laboratories. The array was produced using a 16-level lithographic etching process and contains 40 lenslets each of focal length $f_L = 10$ cm, with no dead space in between (0.635 mm per lenslet). The lenslets divide a single expanded laser beam into 40 subapertures, each of which is focused onto a 50-pixel window of the 2048-pixel CCD array. The location of each of the 40 focal spots is determined by applying a spot locating algorithm to each 50-pixel window. A 5-MHz data acquisition board allows high-resolution detection of the vortical train at a rate of 2.2 kHz. The spatial resolution of the Hartmann sensor is 0.635 mm (the lenslet spacing) along the 2.5-cm sensor axis. The temporal resolution of the measurements is 0.45 ms.

III. Experimental Hartmann Sensor Sensitivity

The sensitivity of the Hartmann sensor was experimentally verified using an optical beam with a spherical phase profile. In the optical system shown in Fig. 2, translating the second lens L_2 of the afocal imaging system by a small distance Δz induces a spherical

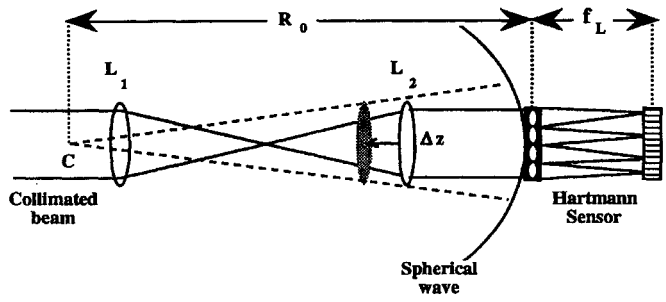

Fig. 2 Optical system to produce a spherical wave emanating from point C with radius of curvature R_0; wave front curvature produced by this system is shown greatly exaggerated.

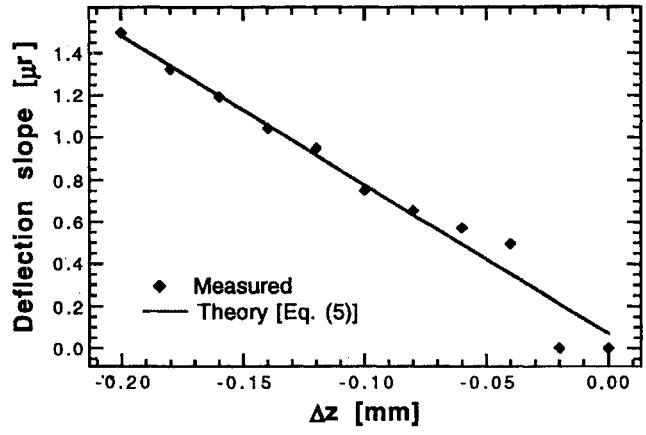

Fig. 3 Slopes of the best least-squares-fit line to deflection data taken at various Δz and theoretical slopes calculated from Eq. (5).

wave that impinges on the lenslet array with a radius of curvature R_0 given by

$$R_0 = -\Delta z - f_2^2/(\beta + \Delta z) \tag{2}$$

where f_2 is the focal length of L_2 and β is the uncertainty in the initial position of L_2. Movement of L_2 toward the left in the figure ($\Delta z < 0$) produces an expanding spherical wave. Movement toward the right ($\Delta z > 0$) results in a converging spherical wave.

The angular tilt experienced by the ith lenslet θ_i due to the spherical wave is given by

$$\tan\theta_i \equiv \theta_i = \xi_i / R_0 \tag{3}$$

Equation (4) shows that for a given spherical wave of radius R_0, the measured tilt is a linear function of position along the sensor array. Combining Eqs. (1–3) and using the lenslet positions $\xi_i = (i - \frac{1}{2})\Delta\xi$ yields an expression for θ_i that is also a linear function of lenslet position,

$$\theta_i = -\left[\frac{\Delta\xi(\beta + \Delta z)}{f_2^2 + \beta\Delta z + (\Delta z)^2}\right]\left(i - \frac{1}{2}\right) \tag{4}$$

The slope of the line describing θ_i is a function of Δz and given by the bracketed quantity in Eq. (4). These slopes are shown as the solid curve in Fig. 7 for $\Delta\xi = 0.635$ mm and $\beta = 0.01$ mm.

The sensitivity of the Hartmann sensor is determined by the smallest tilt differential $\Delta\theta$ that the sensor can measure between successive lenslets. The $\Delta\theta$ are determined from Eq. (4) as

$$\Delta\theta = \Delta\xi / R_{\max} \tag{5}$$

To experimentally determine the smallest detectable tilt of the sensor, lens L_2 was displaced by $\Delta z = -1.0$ mm to produce a diverging spherical wave with $R_0 \approx 450$ m. The magnitude of the displacement was decreased in increments of +0.02 mm until the Hartmann sensor was unable to measure the slope of the line accurately from measurements over its entire length. The measured points in Fig. 3 are the slopes of the best linear fits to the sensor measurements as a

function of Δz. The data diverge significantly from the theoretical points at $\Delta z = 0.08$ mm, corresponding to $R_{max} = 1124$ m. Using this R_{max} and Eq. (5), $\Delta\theta = 0.6\ \mu$r, which represents the sensitivity of the Hartmann sensor.

The effect of environmental noise is effectively removed in this calculation due to the fitting to the linear slopes of data over the entire length of the sensor allowing the theoretical limits of the sensitivity to be reached. When unknown tilt profiles are measured, noise is found to substantially decrease sensitivity. Experimental tilt measurements were taken using the sensor of Fig. 1a without the jet turned on to measure the effect of the environment on the system. Many no-flow measurements were taken under varying ambient laboratory temperatures. These measurements yield an rms noise tilt of approximately 2 μr. For the lenslet array focal length of 10 cm used in our system, lenslet diameter of 0.635 mm and laser wavelength of 633 nm, a 1-μr angular deflection error corresponds to an approximate sensitivity of 0.001 waves. Typical maximum tilt signals (from the flowfield measurements) are on the order of $\pm$50–100 μr.

IV. Noise Characteristics of the Hartmann Sensor in Simulation

The accuracy of wave front measurements made with Hartmann sensors is limited by noise sources associated with CCD cameras. Typically, shot-noise limited Hartmann sensors can measure tilts to within a few thousandths of a wave.[18] This high sensitivity results from the nature of the deflection measurements as relative position measurements of the focal spots with respect to their initial positions. Consequently, slight misalignments and imperfections in the focal spot intensity profile are automatically subtracted provided that the initial spot profiles and positions are well calibrated and misalignments are stationary.

Accuracy of the detector is also subject to errors produced by the algorithms that determine focal spot locations from the intensity pattern recorded on the camera. Simulations of the tilt measurement accuracy in the presence of the electronic read-noise variance of 1.4 mV (saturation = 1 V) and 14-μm-size pixel of the inexpensive EG&G CCD cameras used in the experiments show an rms error in calculated spot location of less than 1 μr. Parameters in the simulation were chosen either to approximate the experimental laboratory sensor or as variable fabrication parameters.

In the simulation of the Hartmann sensor, the lenslet focal spot intensity profile is modeled as a sinc-squared pattern ($\mathrm{sinc}\, x = \sin x/x$) averaged over the 14 μm width of each pixel. The width of the central lobe of the focal spot is determined as a function of the lenslet size and focal length, and each spot is located within a 45-pixel window on the CCD array. Detector noise, which slightly deforms the spots and causes error in the spot location algorithm, is modeled as a zero-mean Gaussian-distributed random process at each pixel that is uncorrelated from pixel to pixel. The variance of the read noise is set to match laboratory observations at 0.15% of the average signal peak. Incoherent interactions between nearest neighbor spots are included in the simulation. The results of simulations that include coherent interactions between the spots do not differ significantly from incoherent results. Since the experiments are run at high-light levels, photon noise is neglected. The length of the array is fixed at 2.5 cm.

The exact (known) position of each spot is selected from a uniform random distribution of angular tilts up to $\pm$30 μr, a value chosen to approximate flow-induced tilt measurements. The Gaussian distributed noise already described is added to noiseless spot intensity profiles. Locations of the noisy spots are calculated using a matched-filter-based algorithm, which in preliminary simulations was found to be more accurate than simple centroiding. To estimate the accuracy of the spot location measurement in the presence of noise, the rms difference is found between spot locations calculated from noisy simulated data and the known set of positions. Predicted sensor performance based on the rms spot location error is plotted as a function of lenslet focal length in Fig. 4 for sensors with 40, 64, and 128 lenslets. It should be noted that the sensor measures spot deflections, that is, the difference between two spot position measurements. If we assume that the spot location error is uncorrelated between these two measurements, then the predicted tilt variance

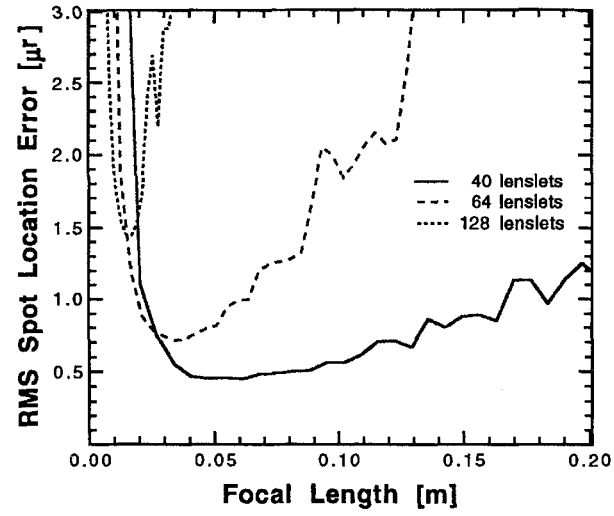

Fig. 4 Spot location error calculated in the Hartmann sensor simulation as a function of lenslet focal length.

will be twice the spot position variance and the rms spot position error is a factor of $\sqrt{2}$ higher than the values given in the plot.

The curves in Fig. 4 show that the current laboratory Hartmann sensor system with 40 lenslets and a focal length of 10 cm is near optimal with a read-noise level of approximately 0.78 μr (note that the factor of $\sqrt{2}$ has been used). The 64- and 128-lenslet Hartmann sensors are shown in the figure for comparison. Modeled sensor behavior agrees well with sensitivity observed in experimental tests on the Hartmann sensor: measurements made over short time periods, when uncorrelated detector noise is expected to dominate and coherent effects are minimized, show rms noise tilts of about 0.7 to 0.9 μr. Over longer runs the sensor typically achieved a sensitivity of 2 μr.

V. Computational Tomography System Design

A multiprojection tomographic system (shown schematically in Fig. 5) has three basic design elements: the number of projections, the number of samples (called lenslets or rays) in each projection, and the focal length (or f-number) of the lenslets in the Hartmann arrays. The number of projections in the design determines the number of Hartmann sensors that are required to operate simultaneously. The number of samples and the lenslet f-number in the design determine how many subapertures each sensor must contain. The complete system design depends on instrumentation noise characteristics as well as flow parameters. The results presented here represent an analysis of computed tomographic (CT) reconstructions produced within a range of practical conditions.

Predicted read-noise levels from Fig. 4 are input to a CT simulation to discern the effects of lenslet size and focal length on the quality of tomographic reconstructions. A truth image for the CT simulation was developed from flow visualization photographs of the jet cross section. In the CT simulation, projections are calculated by computationally propagating laser light rays through the cross-sectional model at specified angles. Each ray corresponds to a lenslet in the Hartmann sensor. Data in a calculated projection consist of the set of OPDs created by the two-dimensional refractive index distribution of the cross-sectional flow model. Noise is then added to the projections as an rms error in the OPD.

In order to calculate the OPD errors from the tilt errors derived in Sec. IV, the method of calculating OPDs from tilt measurements must be considered. The OPD is derived from tilt measurements by integrating the tilt in the forward and backward directions along the array and averaging both results. The OPD given by this average is the sum of N independent random variables, where N is the number of lenslets in the array, and also has zero mean. In addition, if it is assumed that the tilt errors are uncorrelated then the rms error in the OPD σ_{OPD} is given by

$$\sigma_{OPD} = (\Delta\xi\sqrt{N}/2)\sigma_\theta \tag{6}$$

The value of σ_{OPD} is constant over all lenslets in an array.

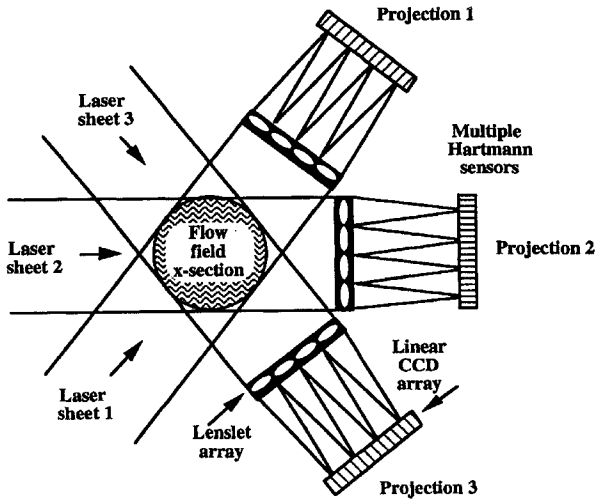

Fig. 5 Multiple Hartmann sensor tomographic system schematic.

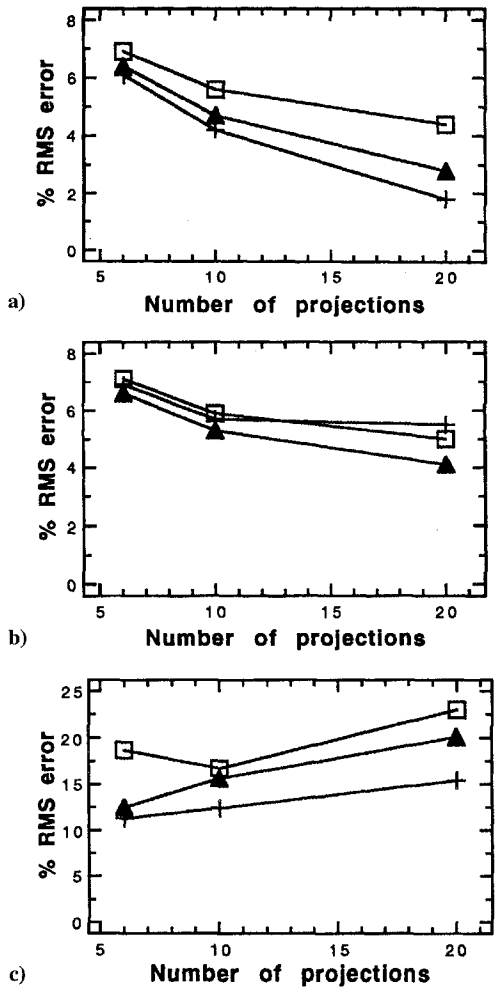

Fig. 6 Percent rms error in tomographic reconstructions for a) noiseless, b) low noise, and c) high-noise projections and + 40, Δ 64, and □ 128 lenslets per projection.

Three levels of noise tilt were considered in the simulation: no read-noise tilt, simulated levels of read-noise tilt shown in Fig. 4, and estimated high-noise tilt. The corresponding σ_{OPD} for these cases for 40-, 64-, and 128-lenslet sensors are shown in Table 1. The resulting quality of image reconstructions from noiseless and noisy data was assessed as a function of the number of projections used in the simulation and the number of lenslets in each projection. Image quality is measured over the entire image using the rms difference between the pixel values of the truth image and the reconstructed image. The rms error is graphed as a function of the number of projections in Fig. 6. From the figure, it is evident that with read noise approximately 9 projections and 64 samples per projection are sufficient to reconstruct an image with 5.5% accuracy. It is interesting to note from Fig. 6b that, although in the noiseless case the tomographic reconstruction improves as the number of rays increases, the 64-lenslet reconstruction is more accurate than the 128-lenslet reconstruction in the presence of simulation noise. This behavior is due to the N dependence in Eq. (6). The optimal focal length corresponding to the 64-lenslet sensor is approximately 4 cm.

Table 1 Noise tilt and noise OPD levels

No. lenslets	Simulation rms tilt, μr	Simulation rms OPD′, μm	High noise rms tilt, μr	High noise rms OPD′, μm
40	0.64	0.0013	6.0	0.012
64	0.99	0.0016	6.0	0.0095
128	2.05	0.0023	6.0	0.0067

This analysis of the tomographic simulation yields three important physical elements of the tomographic design: number of projections, number of samples per projection, and the sensor focal length. An important quantity that is not determined by this analysis is the resolution of the tomographic imaging system. The resolution of the reconstruction process is a function of the number of projections, the number of samples per projection, as well as the size and shape of the area to be reconstructed.[20] In order to capture relevant features in the flowfield cross section, a resolution of at least 2 mm is desirable. Whether the system designed here can reproduce features of this size is at this time being determined using transfer function analysis.

The remaining consideration is the speed of the system. To capture the structure in the flow and its evolution, it is desirable to operate the tomographic system at least 2000 frames/s. For 9 simultaneous projections each containing 2048 8-bit pixels, a data rate of about 300 Mb/s is necessary.

VI. Flowfield Characterization Using the Hartmann Sensor

The Hartmann sensor was used to study the region near the nozzle exit of a low-speed jet flow. The flow generation apparatus consists of a small blower, heating vanes, a plenum with screens and honeycomb, and an 81/1 area-ratio nozzle with exit diameter $D = 2.5$ cm. A complete description of the design may be found in Refs. 21 and 22. The jet axis is oriented vertically and positioned in the center of an optical table that allows unobstructed access around the flow at all angles. For the Hartmann sensor measurements discussed in this paper, the average centerline velocity of the jet U_{CL} is approximately 4 m/s, and the centerline temperature T_{CL} is about 20°C above ambient. Under these conditions the flow has a Reynolds number of about 7000. The Richardson number, which is a measure of the ratio of buoyant to kinetic energy in the flow, of 0.007 indicates that buoyancy effects should be small. The momentum thickness Θ at the nozzle exit plane was measured by constant temperature anemometer (CTA) probe to be 0.36 mm.

The sensor was used in two orthogonal sensor orientations, streamwise and cross stream, which are referred to in normalized units x/D and y/D, respectively. In the streamwise orientation the sensor axis is aligned parallel to the flow axis at various locations above the nozzle exit and centered at $y/D = 0.5$, the geometric edge of the nozzle. The sensor spans an interval along the flow axis equal to $1.0D$, so data acquired at $x/D = 2.0$, for example, span the interval $1.5 \leq x/D \leq 2.5$. The quoted location of the wave front sensor corresponds to the location of the 20th lenslet in the 40-element array. In the cross stream orientation the sensor axis is positioned perpendicular to the jet axis. In this orientation the first lenslet of the array is positioned to capture the wave front passing through the jet axis ($y/D = 0.0$) whereas the 40th lenslet generally intercepted a portion of the wave front that had passed outside the jet. It is the streamwise orientation that most closely resembles the thin-beam jitter geometry in the literature. In all cases the optical beam propagates through the flow in a direction orthogonal to both x and y.

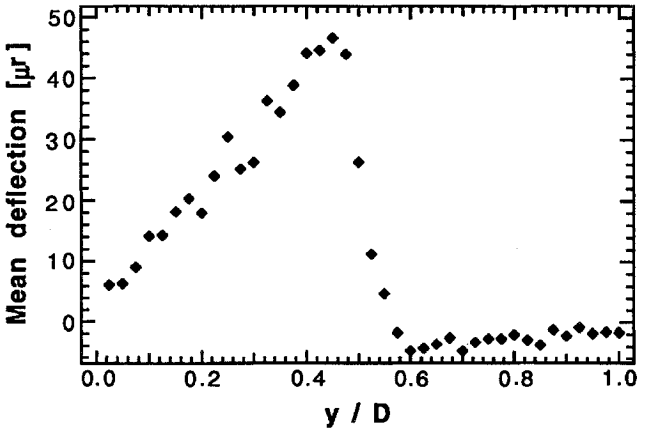

Fig. 7 Time-averaged cross stream deflection measurements of the round jet.

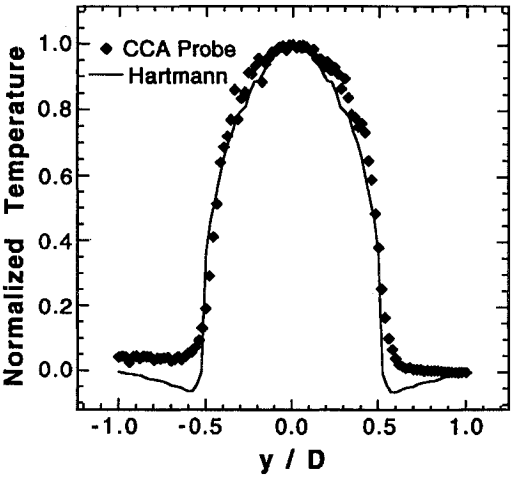

Fig. 8 Abel inversion of data in Fig. 7 (solid line) and temperature probe data vs normalized radial position from the center of the jet.

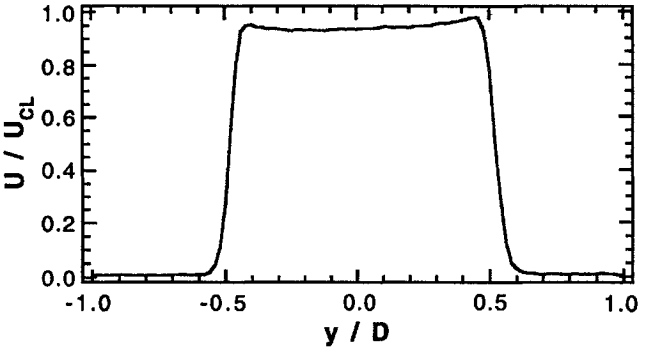

Fig. 9 Velocity profile of jet at $x/D = 0.5$.

Cross Stream Measurements

Near the nozzle exit plane, the cross stream wave front sensor produces a signal with a large dc component upon which a small but readily apparent level of noise is superimposed. At $x/D = 0.5$ eddy formation has not yet occurred and so there is very little temporal variation in the data. The mean deflection signal from each lenslet (time averaged over approximately 100 ms) at $x/D = 0.5$ is shown in Fig. 7. The noise indicated by the lenslet to lenslet jitter in the time-averaged data has an rms level of about 2 μr. The peak deflection of nearly 50 μr is found at the lenslet situated at the edge of the jet near $y/D = 0.5$.

Even though the rays near the jet axis traverse a greater thickness of the round flowfield than those rays farther away from the axis, their deflection is small. Although all optical rays pass through essentially the same interfacial region at the outer edge of the jet, the angle between the ray and the direction of the radial gradient of the flow interface (which is normal to the interface) changes from ray to ray along the sensor. Figure 7 shows that the wave front sensor signal is dominated by the rays that pass through the jet at an angle that is nearly orthogonal to the direction of the gradient. This is also where the refractive index gradients of the flow interface are parallel to the sensor axis. In contrast many interferometry techniques are based on optical path length measurement, which would produce maximum signal near the jet axis where the path lengths are the longest and lose the interfacial gradient information captured by the wave front sensor.

The Abel inversion[23,24] was applied to the data of Fig. 7, and the result is compared to the mean temperature profile of the jet at $x/D = 0.5$ in Fig. 8. The temperature was measured using a 5-μm tungsten wire constant current anemometer (CCA) probe under somewhat different conditions of temperature and flow velocity. This difference of conditions accounts for the necessity of presenting normalized results in Fig. 8. However, the value of the centerline temperature deduced from the wave front sensor agreed to within measurement accuracy of a thermistor probe measurement made immediately prior to the wave front sensor run. In Fig. 9 is shown the CTA probe velocity profile corresponding to the temperature probe data in Fig. 8. Some rounding occurs at the edges of the temperature profile due to the thermal mass of the solid aluminum contraction section, which remained at room temperature during the measurements, as well as cooling near the plenum walls. Also, the plenum turbulence control methodology,[23] based on the conventional screen and honeycomb straightener approach, does little to accomplish the large cross-channel mixing necessary to blend out the temperature nonuniformity that develops in the plenum.

As the wave front sensor is moved downstream, the temporal component of the signal for the deflections becomes larger and eventually dominates the dc component of the signal as shown in Fig. 7. This growth of the temporal component corresponds to the evolving vortical structures in the shear layer around the jet. The vortical structures remain essentially symmetric (toroidal) in this region but exhibit growing longitudinal structure between the rollers.

Figure 10 depicts deflection data taken in the cross stream orientation when the sensor is located at $x/D = 1.0, 2.0$, and 3.0. It is emphasized that these data represent one-dimensional measurements of deflection along the sensor axis direction. The two-dimensional appearance of the data comes from displaying the set of one-dimensional data frames (the abscissa) as a function of time (the ordinate). The images are formed by associating a gray scale with the instantaneous deflection value of the lenslet. In Fig. 10, the vortices can be visualized as being swept by the observer from right to left in the manner of the fluorescence images obtained by Koochesfahani and Dimotakis[25,26] a decade ago. With the entire jet flowfield uniformly illuminated, the wave front sensor data clearly highlight the profile of the jet interface region almost as if the vortices were two-dimensional rather than toroidal, as explained earlier, to the extent that the interior winding of the vortices may be seen. The vortical passage frequency υ is approximately 160 Hz in the image taken at $x/D = 1.0$. The Strouhal number, $Sr_q \equiv U_{CL}\upsilon/\Theta$, computed from this frequency has the value of 0.12 in agreement with the shear layer modal instability found by Zaman and Hussain.[27] Farther downstream, $x/D = 2.0$, the passage frequency halves after vortex pairing has occurred.

Streamwise Measurements

For the streamwise deflection data shown in Fig. 11, the sensor is oriented parallel to the jet axis and located at $x/D = 1.0, 2.0$, and 3.0. Although not synchronous in time, this set of images covers the jet shear layer axially in the complete range $0.5 \leq x/D \leq 3.5$ at $y/D = 0.5$. The diagonal streaks in the images represent the x vs time trajectories of the vortical structures during their convection across the sensor. The average slope of the darkest streaks give an average vortical velocity of $0.56U_{CL}$ in agreement with that educed in Ref. 28.

In the $x/D = 1.0$ deflection image in Fig. 10, shear layer disturbances become visible above the noise floor of the wave front sensor. As these disturbances grow with downstream distance, the temporal

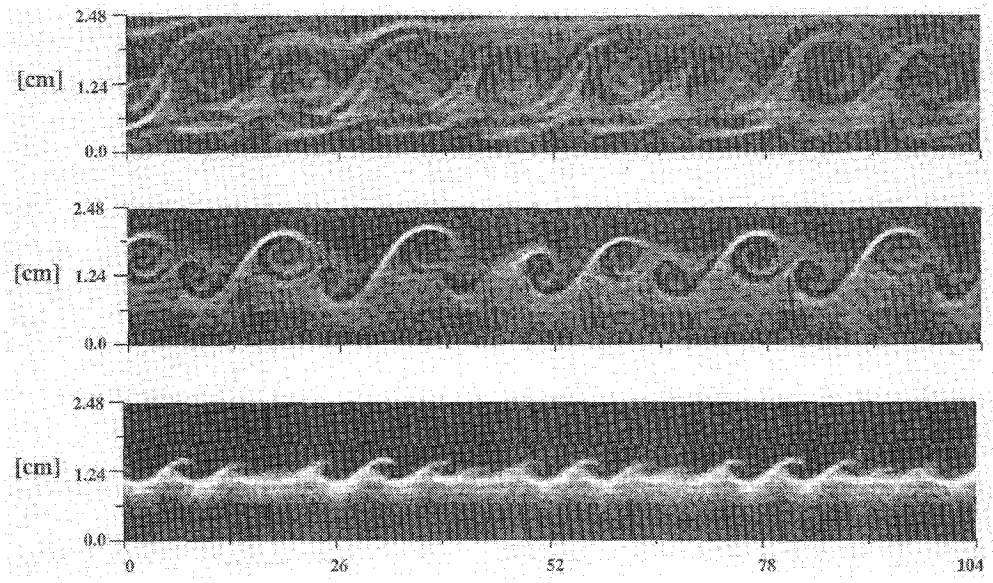

Fig. 10 Cross-stream deflection data acquired at y/D = 1.0, 2.0, and 3.0 (bottom to top).

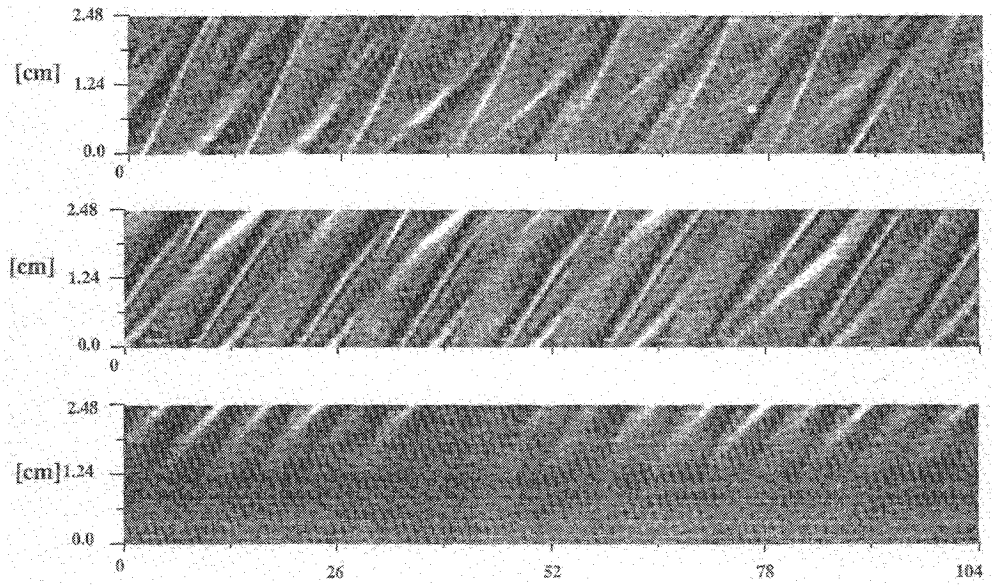

Fig. 11 Streamwise deflection data acquired at y/D = 1.0, 2.0, and 3.0 (bottom to top).

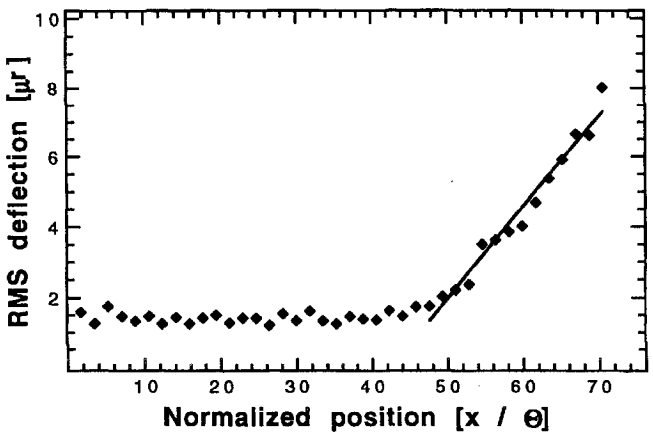

Fig. 12 RMS temporal deflection vs downstream location normalized by Θ.

component of the deflection signal, characterized by its rms amplitude, also grows. Since each lenslet has a different downstream location, we can plot the growth of the temporal component in the downstream direction and compare the result with linear stability theory. A graph of the growth of the rms amplitude vs normalized downstream location is shown in Fig. 11. For small x, the disturbance amplitude is less than the noise floor of the wave front sensor. As x increases, the oscillation amplitude increases in an exponential fashion, as expected for disturbances in the linear regime. The 14 data points farthest downstream were selected as being sufficiently above the noise floor to provide a reliable determination of the amplification rate. A least squares fit gave the value of amplification rate as 0.06534. The value agrees quite well with the range of values suggested by Ho and Huerre[28] in their review of the jet free shear layer.

VII. Conclusions

We have shown that one-dimensional Hartmann sensing is a powerful technique for investigating the structure of flowfields. Although closely related to the beam deflection techniques used in previous

turbulence investigations, Hartmann sensing offers the advantages of controllable sensitivity and high-spatial resolution. Simulations and experimental measurements of the sensitivity of the sensor were presented. The theoretical sensitivity of the Hartmann sensor was estimated using an extensive simulation that included the effects of detector noise and nearest neighbor spot interactions in the focal plane. The 40-subaperture sensor used in the experiments was estimated to have an angular tilt sensitivity of less than 1 μr and achieved an actual sensitivity of 2 μr in noisy laboratory conditions.

Because of the high spatial and temporal resolution of the Hartmann sensor measurements a one-dimensional sensor can provide two-dimensional space-time plots of flow structure that resemble flow visualization (Figs. 10 and 11) by associating a gray scale value with deflection amplitude. From the one-dimensional measurements taken using the streamwise orientation of the sensor we have calculated average convection velocity and amplification rate that agree with expected results for this type of flow in the literature. From one-dimensional cross stream measurements, we have obtained accurate measurements of the vortical passage frequency both before and after vortex pairing has occurred.

Unlike hot-wire probe and other intrusive local measurement techniques, beam-deflection flow measurements are necessarily integrated along the entire optical path through the flow. However, interior winding of the eddy structure is still apparent in the path-integrated cross stream Hartmann measurements (Fig. 10) due to the sensitivity of the sensor measurements to the gradients (or interface regions) in the flow. A direct comparison of hot-wire measurements and Hartmann sensor data showing good agreement was accomplished using the Abel transform (Fig. 9) with the implicit assumption of axisymmetric flow. In combination with tomographic reconstruction techniques, a set of simultaneously operating Hartmann sensors should be able to measure interior structure of flow without the assumption of axisymmetry.

Acknowledgments

This work was sponsored by the Air Force Office of Scientific Research, Air Force Materiel Command, U.S. Air Force. We would like to thank Daniel R. Neal for the use of the linear Hartmann sensor hardware, binary optics, and software technology developed at Sandia National Laboratories, Albuquerque, New Mexico.

References

[1]Schack, R. V., "Direct Phase Sensing Interferometer," *Journal of the Optical Society of America*, Vol. 61, No. 5, 1971, p. 655.

[2]Schack, R. V., and Platt, B. C., "Production and Use of a Lenticular Hartmann Screen," *Journal of the Optical Society of America*, Vol. 61, No. 5, 1971, p. 656.

[3]Paschereit, C. O., Wygnanski, I., and Fiedler, H. E., "Experimental Investigation of Subharmonic Resonance in an Axisymmetric Jet," *Journal of Fluid Mechanics*, Vol. 283, 1995, pp. 365–407.

[4]Fugate, R. Q., "Measurement of Atmospheric Distortion Using Scattered Light from a Laser Guidestar," *Nature*, Vol. 353, Sept. 12, 1991, pp. 144–146.

[5]Thompson, L. A., "Adaptive Optics in Astronomy," *Physics Today*, Vol. 47, No. 12, 1994, pp. 24–31.

[6]McMackin, L., Wissler, J., Clark, N., Chen, E., Bishop, K., Pierson, R., and Staveley, B., "Hartmann Sensor and Dynamic Tomographical Analysis of Organized Structure in Flow Fields," AIAA Paper 94-2548, June 1994.

[7]Santoro, R. J., Semerjian, H. G., Emmerman, P. J., and Goulard, R., "Optical Tomography for Flow Field Diagnostics," *International Journal of Heat Mass Transfer*, Vol. 24, No. 7, 1981, pp. 1139–1150; also AIAA Paper 80-1541, July 1980.

[8]Faris, G. W., and Byer, R. L., "Three-dimensional Beam Deflection Optical Tomography of a Supersonic Jet," *Applied Optics*, Vol. 27, No. 24, 1988, pp. 5202–5212.

[9]Watt, D. W., and Vest, C. M., "Turbulent Flow Visualization by Interferometric Integral Imaging and Computed Tomography," *Experiments in Fluids*, Vol. 8, 1990, pp. 301–311.

[10]Beiting, E. J., "Fiber-Optic Fan Beam Absorption Tomography," *Applied Optics*, Vol. 31, No. 9, 1992, pp. 1328–1343.

[11]Snyder, R., and Hesselink, L., "High Speed Optical Tomography for Flow Visualization," *Applied Optics*, Vol. 24, No. 23, 1985, pp. 4046–4051; also "Measurement of Mixing Fluid Flows with Optical Tomography," *Optics Letters*, Vol. 13, No. 2, 1988, pp. 87–89.

[12]Gmitro, A. F., and Gindi, G. R., "Computed Tomography Videography: an Electrooptical System for Video-rate Image Reconstruction," *Applied Optics*, Vol. 24, No. 23, 1985, pp. 4040–4045.

[13]Malley, M. M., Sutton, G. W., and Kincheloe, N., "Beam-jitter Measurements of Turbulent Aero-optical Path Differences," *Applied Optics*, Vol. 31, No. 22, 1992, pp. 4440–4443.

[14]Jumper, E. J., and Hugo, R. J., "Optical Phase Distortion Due to Turbulent Fluid Density Fields: Quantification Using the Small-aperture Beam Technique," AIAA Paper 92-3020, July 1992.

[15]Kalghati, G. T., "A Study of Coherent Structures in Axisymmetric Jets Using an Optical Technique," *AIAA Journal*, Vol. 18, No. 3, 1980, pp. 225, 226.

[16]Wissler, J. B., and Roshko, A., "Transmission of Thin Beams Through Turbulent Mixing Layers," AIAA Paper 92-0658, Jan. 1992.

[17]Neal, D. R., O'Hern, T. J., Torczynski, J. R., Warren, M. E., and Shul, R., "Optical Diagnostics in Fluid and Thermal Flow," Society of Photo-Optical Instrumentation Engineers, *SPIE Proceedings*, Vol. 2005, 1993, pp. 194–203.

[18]Kwo, D., Damas, G., and Zmek, W., "A Hartmann-Shack Wavefront Sensor Using a Binary Optic Lenslet Array," Society Photo-Optical Instrumentation Engineers, *SPIE Proceedings*, Vol. 1544, 1991, pp. 66–74.

[19]Tyson, R. K., *Principles of Adaptive Optics*, Academic, Boston, MA, 1991, Chaps. 5 and 7.

[20]Joseph, P. M., Spital, R. D., and Stockham, C. D., "The Effects of Sampling on CT Images," *Computerized Tomography*, Vol. 4, 1980, pp. 189–206.

[21]Truman, C. R., Zadocks, R. I., Staveley, B. D., and Barsun, H., "Prediction and Measurement of Aero-optic Effects Through the Dynamics of a Passive Scalar in a Turbulent Shear Flow," AIAA Paper 94-2549, June 1994.

[22]Staveley, B. D., "Optical Investigation of the Turbulent Scales in a Round Jet," M.S. Thesis, Dept. of Mechanical Engineering, Univ. of New Mexico, Albuquerque, NM, 1994.

[23]Bracewell, R. N., *The Fourier Transform and its Applications*, 2nd ed., McGraw–Hill, New York, 1978.

[24]Masson, B., McMackin, L., Wissler, J., and Bishop, K., "Study of a Round Jet Using a Shack–Hartmann Wavefront Sensor," AIAA Paper 95-0644, Jan. 1995.

[25]Koochesfahani, M. M., and Dimotakis, P. E., "Laser Induced Fluorescence Measurements of Mixed Fluid Concentration in a Liquid Plane Shear Layer," *AIAA Journal*, Vol. 23, No. 11, 1985, pp. 1700–1707.

[26]Koochesfahani, M. M., and Dimotakis, P. E., "Mixing and Chemical Reactions in a Turbulent Liquid Mixing Layer," *Journal of Fluid Mechanics*, Vol. 170, 1986, pp. 83–122.

[27]Zaman, K. B. M. Q., and Hussain, A. K. M. F., "Vortex Pairing in a Circular Jet Under Controlled Excitation. Part 1. General Jet Response," *Journal of Fluid Mechanics*, Vol. 101, 1981, pp. 449–491.

[28]Ho, C. M., and Huerre, P., "Perturbed Free Shear Layers," *Annual Review of Fluid Mechanics*, Vol. 16, 1984, pp. 365–424.